CrossMark

A Magnetically Driven Disk Wind in the Inner Disk of PDS 70[*]

Justyn Campbell-White[1] , Carlo F. Manara[1] , Myriam Benisty[2,3] , Antonella Natta[4], Rik A. B. Claes[1] , Antonio Frasca[5] ,
Jaehan Bae[6] , Stefano Facchini[7] , Andrea Isella[8] , Laura Pérez[9] , Paola Pinilla[10] , Aurora Sicilia-Aguilar[11] , and
Richard Teague[12]
[1] European Southern Observatory, Karl-Schwarzschild-Strasse 2, D-85748 Garching bei München, Germany; jcampbel@eso.org
[2] Université Côte d'Azur, Observatoire de la Côte d'Azur, CNRS, Laboratoire Lagrange, F-06304 Nice, France
[3] Université Grenoble Alpes, CNRS, Institut de Planétologie et d'Astrophysique (IPAG), F-38000 Grenoble, France
[4] Dublin Institute for Advanced Studies, 31 Fitzwilliams Place, Dublin, Ireland
[5] INAF—Osservatorio Astrofisico di Catania, via S. Sofia, 78, I-95123 Catania, Italy
[6] Department of Astronomy, University of Florida, Gainesville, FL 32611, USA
[7] Dipartimento di Fisica, Università degli Studi di Milano, via Celoria 16, I-20133 Milano, Italy
[8] Department of Physics and Astronomy, Rice University, 6100 Main Street, MS-108, Houston, TX 77005, USA
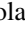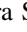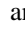[9] Departamento de Astronomía, Universidad de Chile, Camino El Observatorio 1515, Las Condes, Santiago, Chile
[10] Mullard Space Science Laboratory, University College London, Holmbury St Mary, Dorking, Surrey RH5 6NT, UK
[11] SUPA, School of Science and Engineering, University of Dundee, Nethergate, DD1 4HN, Dundee, UK
[12] Department of Earth, Atmospheric, and Planetary Sciences, Massachusetts Institute of Technology, Cambridge, MA 02139, USA
Received 2023 July 3; revised 2023 August 11; accepted 2023 August 14; published 2023 October 4

Abstract

PDS 70 is so far the only young disk where multiple planets have been detected by direct imaging. The disk has a large cavity when seen at submillimeter and near-infrared wavelengths, which hosts two massive planets. This makes PDS 70 the ideal target to study the physical conditions in a strongly depleted inner disk shaped by two giant planets, and in particular to test whether disk winds can play a significant role in its evolution. Using X-Shooter and HARPS spectra, we detected for the first time the wind-tracing [O I] 6300 Å line, and confirm the low-moderate value of mass-accretion rate in the literature. The [O I] line luminosity is high with respect to the accretion luminosity when compared to a large sample of disks with cavities in nearby star-forming regions. The FWHM and blueshifted peak of the [O I] line suggest an emission in a region very close to the star, favoring a magnetically driven wind as the origin. We also detect wind emission and high variability in the He I 10830 Å line, which is unusual for low accretors. We discuss that, although the cavity of PDS 70 was clearly carved out by the giant planets, the substantial inner-disk wind could also have had a significant contribution to clearing the inner disk.

Unified Astronomy Thesaurus concepts: Protoplanetary disks (1300); Classical T Tauri stars (252); Weak-line T Tauri stars (1795); Stellar accretion disks (1579); Variable stars (1761); High resolution spectroscopy (2096)

1. Introduction

The search for planets around young stellar objects (YSOs) during the planet formation stage is still an ongoing challenge in astronomy. So is the cause and evolution of the various disk substructures that are now ubiquitously observed around YSOs (e.g., Andrews 2020; Benisty et al. 2022). Although it could be assumed that such substructures are exclusively the direct result of embedded protoplanets, this assumption does not match with the observed exoplanet population (e.g., Lodato et al. 2019).

While the simple reasoning for disk substructures is pressure perturbations in the disk, the physical source can theoretically be explained not only by planets, but also by thermal, magnetohydrodynamic (MHD) and gravitational fluid instabilities within the disk material (for a review, see Bae et al. 2022). Cavities in the inner disk caused by substantial mass loss may be the result of MHD (Takahashi & Muto 2018) or photoevaporative winds (Alexander et al. 2014). Consecutive

gaps in the disks could also be the result of magnetic field concentrations within the disk, inherent in MHD zonal flows (Flock et al. 2017; Riols & Lesur 2019; Riols et al. 2020). Photoevaporation could be responsible for inner-disk depletion (e.g., Gárate et al. 2021); however, this effect alone may not be strong enough to form the large cavities we observe in some transition disks (TDs; Owen 2016; Picogna et al. 2019).

In order to observationally disentangle the influence of disk winds on the creation of disk substructures, we should first understand whether there is any traces of a disk wind in systems where we are certain the large cavity is due to the presence of protoplanets. We may then be able to look to how such disk winds can differ or enhance the effects of substructure formation due to embedded planets (e.g., Aoyama & Bai 2023; Wafflard-Fernandez & Lesur 2023).

PDS 70, a young (5.4 Myr; Pecaut & Mamajek 2016), nearby (~112 pc; Gaia Collaboration et al. 2021) star is so far the only system hosting multiple directly imaged forming planets. A large cavity hosting two massive protoplanets has been observed from submillimeter to near-infrared (NIR) observations (e.g., Keppler et al. 2018; Haffert et al. 2019; Benisty et al. 2021). For the central star, Hα equivalent width (EW) and UV flux measurements classed PDS 70 as a nonaccreting weak-line T-Tauri star (WTTS; Gregorio-Hetem & Hetem 2002; Joyce et al. 2020). However, further analysis

---
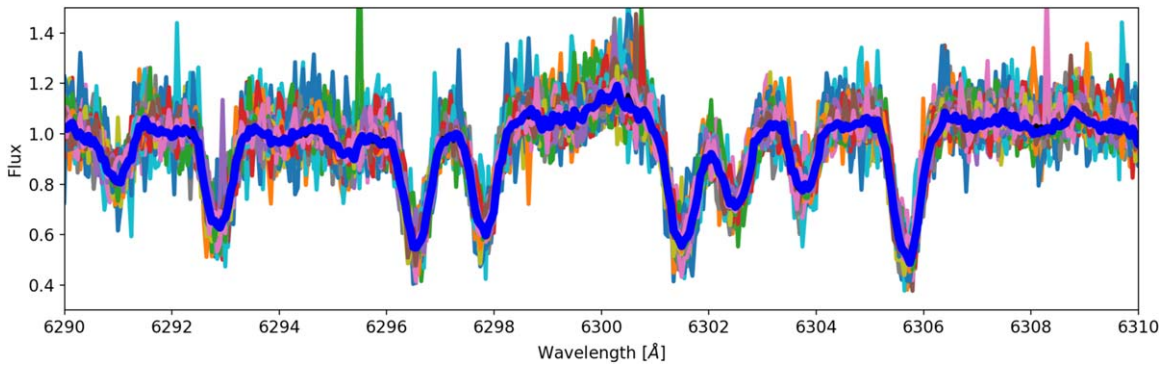
Figure 1. 47 HARPS epochs of PDS 70 shown in background colors, with median combined spectra shown in thick blue. Flux is scaled to the local continuum and centered around the position of [O I] 6300 Å.

with magnetospheric modeling of the Hα line, accounting for chromospheric contributions, revealed a variable low to moderate accretion rate of 0.6–$2.2 \times 10^{-10} M_\odot \, \mathrm{yr}^{-1}$ (Thanathibodee et al. 2020) with an inverse P-Cygni profile appearing and disappearing with the same periodicity as the stellar rotation. Observations with the Space Telescope Imaging Spectrograph (STIS) of the Hubble Space Telescope (HST) confirmed both a significant chromospheric contribution from various UV emission lines and similar accretion rate with measurement of the accretion-sensitive C IV line (Skinner & Audard 2022). They also revealed the presence of fluorescent H$_2$ in the UV spectra, which is unusual for WTTSs and would be pumped by Lyα emission. Thanathibodee et al. (2020) also presented a low-resolution He I 10830 Å profile that is indicative of both accretion and a wind.

The observed X-ray and ultraviolet (XUV) luminosity of PDS 70 suggests there should be a photoevaporative mass loss driven by this ionizing radiation, which is potentially observable by disk-wind tracers. This was suggested by Joyce et al. (2020) from analysis of the SWIFT observations, where they predict a mass-loss rate $\sim 10^{-8} M_\odot \, \mathrm{yr}^{-1}$. These XUV measurements were later confirmed with follow-up XMM-Newton observations in Joyce et al. (2023). Given this substantial mass-loss rate, the disk would be dispersed in less than ~ 1 Myr. However, this is for a total disk mass of 10^{-2}–$10^{-3} M_\odot$ (Keppler et al. 2018), assuming the typical dust-to-gas ratio of 100, and that the photoionization is efficient in reaching the outer disk. It may be that the inner disk is more optically thick than previously thought, as shown by Benisty et al. (2021), which would not allow all of the XUV flux to reach the outer disk. Study of the HST STIS spectra also suggested such photoevaporation only impacts the inner disk, with the planets and outer disk shielded until the inner disk is dissipated (Skinner & Audard 2022). This study also predicts a more modest mass-loss rate on the order of $\sim 10^{-10} M_\odot \, \mathrm{yr}^{-1}$, based on the C IV luminosity.

If such photoevaporation or an MHD disk wind is present in the system, it may be detectable from forbidden emission lines. It is well established that such emission is a direct tracer of outflowing material from the star and disk (Pascucci et al. 2023), be it high-velocity jets (e.g., Hartigan et al. 1995; Nisini et al. 2018) or lower velocity disk winds (e.g., Rigliaco et al. 2013; Natta et al. 2014; Fang et al. 2018). Lines such as [O I] 6300 Å have been spectrally resolved into velocity components, with models suggesting different physical origins (e.g., Weber et al. 2020); however, it remains difficult to conclusively disentangle such origins i.e., thermal, nonthermal, or

magnetic (Nemer et al. 2020). Recent work has suggested that most, if not all of the low-velocity emission should be due to MHD winds (e.g., Simon et al. 2016; McGinnis et al. 2018; Banzatti et al. 2019; Fang et al. 2023). Banzatti et al. (2019) further showed that the presence of a cavity in the disk results in no high-velocity component, with narrower [O I] lines produced in more depleted cavities.

In this work, we present analysis of medium- and high-resolution spectra of PDS 70, which are detailed in Section 2. We present confirmation of the accretion-rate measurements from these data in Section 3, along with extraction of disk-wind-tracing emission lines. These results are then compared to those of other Class II stars, WTTSs, and TDs and further discussed in Section 4. We then report our conclusions in Section 5.

2. Observations and Data Reduction

PDS 70 was observed twice with the X-Shooter instrument (Vernet et al. 2011) on the ESO Very Large Telescope (VLT) in 2020 December and 2021 February (Pr. ID: 105.205R, PI Benisty). These were medium-resolution spectral observations, simultaneously covering three wavelength ranges UV-blue (~ 300–560 nm), visible (VIS; ~ 560–1024 nm), and NIR (~ 1020–2480 nm). We note a small variability in the continuum flux levels for each epoch. For further information and data reduction, see Appendix A.

PDS 70 was previously observed over multiple seasons by the High Accuracy Radial velocity Planet Searcher (HARPS; Mayor et al. 2003) on the ESO 3.6 m telescope at La Silla (Pr. IDs: 098.C-0739, 0104.C-0418, 1101.C-0557, PI Lagrange). HARPS has a high spectral resolution of R = 115,000, with a spectral coverage of 3780–6910 Å. Data were reduced by the HARPS pipeline, which removes sky emission using the other fiber. We then removed telluric absorption features with a developmental version of the molecfit software.[13] These data included 32 observations from 2018, four from 2019, and 11 from 2020, totaling 47 epochs. A summary of observations is shown in Appendix B.

To vastly improve the signal-to-noise of the observations, we median combined all 47 HARPS epochs. The continuum normalized region around $\lambda = 6300$ Å is shown in Figure 1, with this median combined spectra highlighted. Median combining also helped to smooth a few cases of residual noise around the weak sky line that is subtracted from the science

---

[13] https://support.eso.org/kb/articles/molecfit-experimental-version
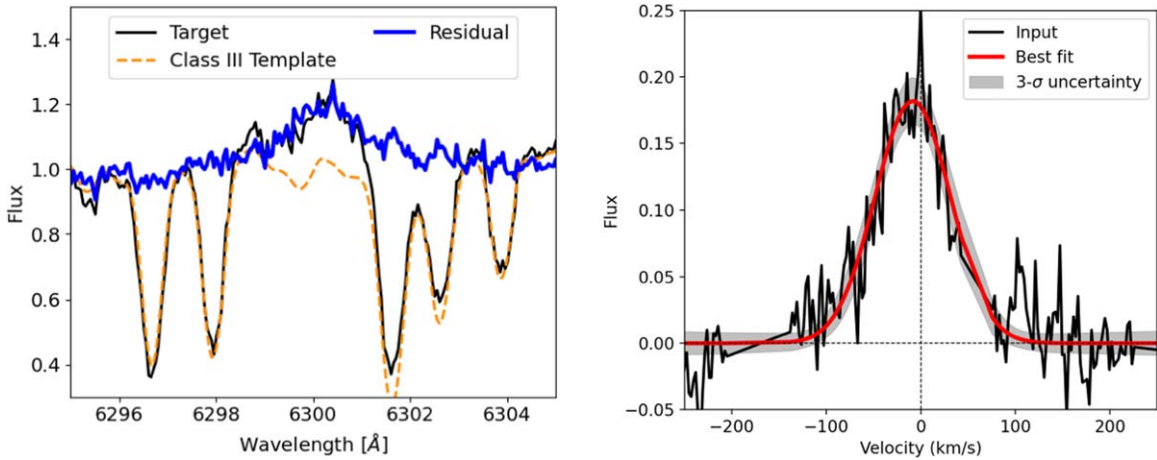
Figure 2. Left: photosphere removal around the [O I] 6300 Å line of the median combined HARPS spectra (black) with a WTTS template (orange). Resultant residual subtraction of the template from the target is shown in blue. Flux values are scaled to the local continuum. Right: corresponding best-fit model to the continuum flux subtracted [O I] line.

spectra. Each epoch is already barycentric corrected by the HARPS pipeline. We measure a low dispersion of radial velocity values across individual observations, with a 1σ spread of $0.8\,\mathrm{km\,s^{-1}}$ and typical individual measurement standard errors of $0.03\,\mathrm{km\,s^{-1}}$. The wavelength values were hence not corrected for individual radial velocities before combination. All subsequent kinematic calculations are adjusted for the average stellar radial velocity value that we determine of $5.5\,\mathrm{km\,s^{-1}}$. Radial velocity measurements and subsequent emission line analysis for this work were carried out using the STAR-MELT Python package (Campbell-White et al. 2021).[14]

3. Analysis

3.1. Accretion-rate Measurements

We first sought to confirm the accretion-rate measurements of PDS 70 from those previously determined using magnetospheric modeling of the Hα emission (Thanathibodee et al. 2020). Using the flux-calibrated X-Shooter observations, we attempted a fit following the procedure as described by Manara et al. (2013a), whereby a nonaccreting Class III template, reddening and, a slab model are used to estimate the observed UV continuum excess, directly resulting from the accretion. However, there is essentially zero UV excess for PDS 70, so the accretion rates obtained from this method were overestimated. This was apparent from comparison of prominent photospheric absorption lines, such as Ca II $\lambda = 423$ nm, being too highly veiled in the fit with a slab model. Fitting the PDS 70 spectrum using only a nonaccreting Class III K7 template and no slab did accurately represented such photospheric features. This is due to the fact that accretion in this target, if any, is too low to be detected as continuum excess. Since we detect multiple accretion tracing emission lines in the PDS 70 spectra, we therefore use the other well studied method of determining the accretion using the line luminosity—accretion luminosity correlations (Alcalá et al. 2017).

Emission lines detected in the PDS 70 X-Shooter and HARPS spectra include those from the hydrogen Balmer series, Ca II H and Ca II K. The Ca II H line is resolved from the

adjacent Hε line in the higher-resolution HARPS spectra. We do not detect He I in the optical, nor the Paschen nor Brackett lines in the NIR. The Ca II IR triplet is detected but is deeply embedded in the photospheric absorption lines. Further details of the line flux measurements and determined accretion luminosities are given in Appendix C.

The mean accretion luminosity we derive from the emission lines is $\log(L_{\mathrm{acc}}/L_{\odot}) = -2.88 \pm 0.11$. Given the stellar mass ($0.76\,M_{\odot}$, Müller et al. 2018) and radius ($1.26\,R_{\odot}$, Pecaut & Mamajek 2016) of PDS 70, this corresponds to an accretion rate of $\log(\dot{M}_{\mathrm{acc}}\,\mathrm{yr}^{-1}) = -10.06 \pm 0.11$. Since we used the mean HARPS spectra across all epochs, this result is in good agreement with the range of accretion-rate values calculated by Thanathibodee et al. (2020).

3.2. Wind-tracing Emission Lines

We performed photospheric subtraction around the potential wind-tracing forbidden emission line positions using a Class III template, RXJ1543.1-3920. This template spectra was obtained as part of the PENELLOPE large program on the ESO Very Large Telescope, using the ESPRESSO instrument (for details of the reduction, see Manara et al. 2021); hence, no spectral degrading was required due to the high resolution of the template. Following the standard procedure, the target spectra and photospheric template spectra were continuum normalized. The template spectra was then shifted and broadened to respectively match the radial velocity (RV) and projected rotational velocity ($v \sin i$) of the target spectra. For PDS 70, no absorption line veiling is present. The fit resulting in the smallest residuals around the [O I] 6300 Å line (from both χ^2 calculations and visual inspection) is shown in Figure 2 left.

Figure 2 right shows the first detection of the resulting [O I] 6300 Å emission line and best-fit model. The signal-to-noise ratio (S/N) of this detection from the combined HARPS spectra is 9.5. We calculate an EW of -0.44 Å, which, together with the X-Shooter continuum flux measurement of $4.7 \pm 0.3 \times 10^{-13}$ erg s^{-1} cm^{-2} nm^{-1}, gives an integrated line flux of $2.1 \pm 0.4 \times 10^{-14}$ erg s^{-1} cm^{-2}. This corresponds to a line luminosity of $\log(L_{\mathrm{[OI]}}/L_{\odot}) = -5.08 \pm 0.15$. We checked whether fewer combined spectra yields the same line luminosity results, and find consistent EWs across each year of observations, but with lower S/Ns and higher errors on

---

corresponding model fits. We do also detect the [O I] 6300 Å line in the X-Shooter spectra, with an S/N of 8 using a median combination of the two epochs. Due to the lower resolution, the photospheric removal results in a poorer subtraction with more prominent residuals either side of the emission; however, we are still able to measure the EW of -0.46 Å, providing a line luminosity in good agreement with the HARPS data. The lower resolution of the X-Shooter data is also not as suitable for kinematic line analysis. The remainder of the analysis is hence carried out on the total combined HARPS spectra.

The [O I] 6363 Å line, which is a factor of 3 weaker than the [O I] 6300 Å line, is within a region of the spectra more significantly affected by photospheric absorption features. We were able to measure the EW of this line above the continuum, finding a value of -0.16 Å but with an S/N of 3.1. This is consistent with the expected ratio. However, this low S/N does not allow for further analysis of this line. No further forbidden emission lines, such as [S II] or [N II] were detected in the photospheric removed HARPS spectra, neither was the [O I] 5577 Å. We also note that there is no trace of [Ne II], as shown in Perotti et al. (2023).

For the best-fit model to the [O I] 6300 Å emission line, the line intensity is strong enough with respect to the local continuum such that small residual artifacts from the adjacent photospheric removals have negligible effects on the fit. We find consistent fit results when checking fewer combined epochs and subsequent photospheric removals, as with the consistent line luminosity measurements previously noted. A single Gaussian low-velocity component (LVC) is adequate to model the line. A linear component was added to the Gaussian component to model the local continuum, as described in Campbell-White et al. (2021). This results in a more accurate fit to the emission component, allowing for slight asymmetries in the overall fit. A combination of broad and narrow component fit could be adopted for this line, but this does not significantly improve the goodness of fit of the model and hence is not adopted (following the criteria by Banzatti et al. 2019). From this best-fit single Gaussian model, the central velocity of the Gaussian component (V_p) is -8 ± 2 km s^{-1} (accounting for the standard error of the Gaussian fit, plus the spread in RV values), and the FWHM is 89 ± 5 km s^{-1}. The 3σ errors of the fit are shown in Figure 2 right.

We also detect the He I 10830 Å emission line from each X-Shooter spectrum, which shows blueshifted absorption, indicative of a wind, plus redshifted emission. These observed profiles are strikingly different to the one presented in Thanathibodee et al. (2020), which shows both blue and redshifted absorption components. We checked the alignment between the VIS and NIR arm of the X-Shooter data using overlapping photospheric lines to ensure no velocity offsets, as noted in Erkal et al. (2022). This line and interpretation of the [O I] are discussed further in the next section, where we compare properties of the [O I] emission to those of other YSOs and the He I profile to the previous observation.

4. Discussion

With this first detection of [O I] emission from PDS 70, we can compare the measured stellar and line properties to those of other Class II YSOs, TDs, and WTTSs. Literature data of YSOs from nearby star-forming regions were taken from Manara et al. (2014) for TDs; Nisini et al. (2018) for all Class II disk types; Fang et al. (2018) for TDs; and Fang et al. (2023) for all
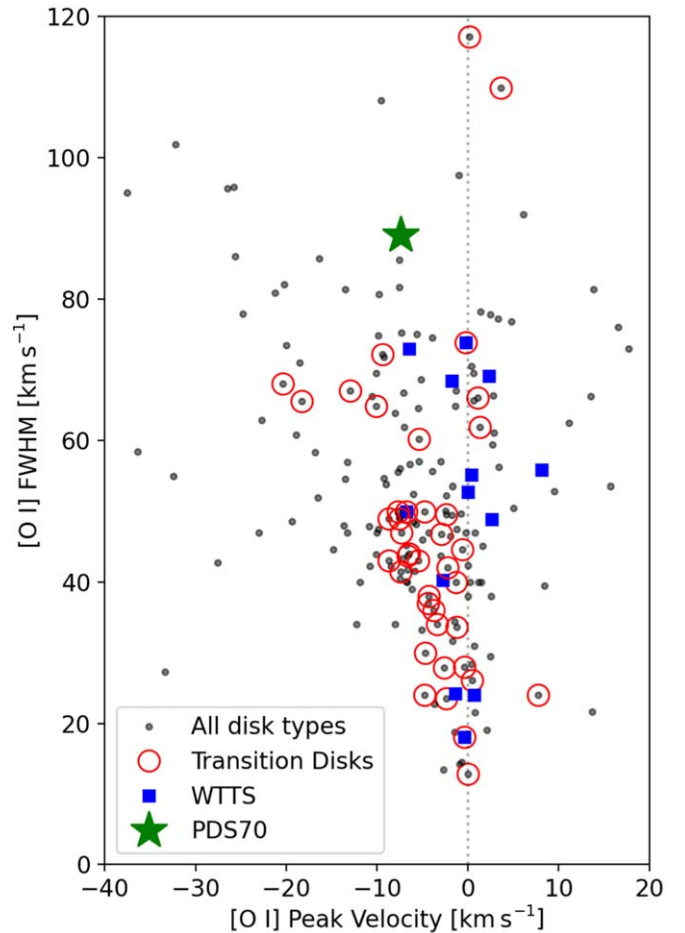
Figure 3. [O I] 6300 Å peak velocity vs. FWHM comparing the values we obtain for the fit of PDS 70 to those of other YSOs from the literature values of Manara et al. (2014), Nisini et al. (2018), Fang et al. (2018), and Fang et al. (2023). Points show Class II sources, with TDs indicated by the red circles; blue squares show WTTSs from Upper Sco with detected [O I]. The values we obtained from the best fit of the PDS 70 [O I] is indicated by the green star.

disk types. All of the WTTS measurements are taken from this final study and are targets in Upper Sco; hence, they should also have similar ages to PDS 70. We include this comparison given its classification as a WTTS based on the Hα profile. However, there are noteworthy discrepancies between both measurements of the emission lines (previously due to spectral resolution, also variability), and the method used to define the WTTS class (e.g., via He I instead of Hα, Thanathibodee et al. 2022). Many WTTSs still possess low-moderate accretion rates; however, this is difficult to distinguish from chromospheric noise (Manara et al. 2013b).

4.1. [O I] Kinematics

Figure 3 shows the kinematic values for the fits to the [O I] lines: central velocity, V_p, and FWHM. For stars with all disk types that have a multicomponent fit to the [O I], only the LVC kinematic values are shown. All TDs and WTTSs included from previous studies have a single component fit. Typical velocity errors are reported similar to those we measure here, with those from lower-resolution surveys still <10 km s^{-1}. It is clear from Figure 3 that both the TDs and WTTSs occupy a smaller parameter space than other Class II disks. PDS 70 is clearly an outlier from the WTTS sample. For the TDs, the
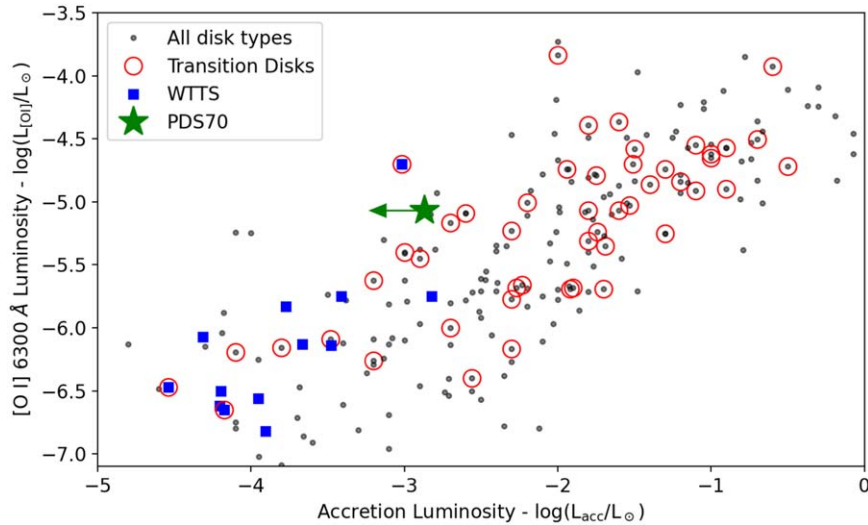
Figure 4. [O I] 6300 Å line luminosity vs. accretion luminosity for PDS 70 and literature values. The accretion luminosity value of PDS 70 is as we measure from the average HARPS spectra emission lines. Markers and colors and the same as Figure 3, as are the sources of literature values.

mean FWHM is ∼48 km s^{-1}. The value obtained for PDS 70 is ∼2σ away. Only two TDs have higher FWHMs (SZ 65 and IM Lup; Fang et al. 2018).

The fact that the peak is slightly blueshifted is in agreement with models of disk winds (Ercolano & Owen 2010; Weber et al. 2020; Ercolano & Picogna 2022). Assuming Keplerian rotation ($\Delta v = \sin(i)\sqrt{GM_\star/R}$), a disk inclination, i, of 50° (Thanathibodee et al. 2020) and using the FWHM of the profile to approximate the broadening velocity, Δv (e.g., Banzatti & Pontoppidan 2015; Simon et al. 2016; Fang et al. 2018), scaled by the stellar mass ($0.76 \pm 0.02\ M_\odot$, Müller et al. 2018), we estimate an emitting radius of ∼0.1–0.2 au for the [O I]. Since this emitting region is well within the gravitationally bound part of the disk, this also suggests the [O I] is tracing a magnetically driven wind rather than photoevaporative. Due to the degeneracies of the Gaussian fitting, it is still possible that two components of the [O I] are present, with a narrow component tracing a photoevaporative wind from further out in the disk. However, with this type of composite model, the broad component would be even broader, corresponding to emission from just above the stellar surface and not necessarily the disk.

B. Nisini et al. (in preparation) find a tentative anticorrelation between the Keplerian emitting region of the [O I] and the inner cavity size for TDs. This is opposite to what was found in Banzatti et al. (2019) for the correlation with single component LVC fits and spectral index at 13–31 μm, which is used as a proxy for dust in the inner circumstellar disk region. The results from Banzatti et al. (2019) show that the LVC FWHM decreases as the inferred cavity size increases; however, this assumption was only from the spectral index, and not from direct cavity size measurements. It is possible that once the inner cavity forms, the [O I] emission moves inward toward higher-density regions of the inner disk as the dust depletion region increases (B. Nisini et al., in preparation). What we find here for PDS 70 supports this hypothesis, with the emission originating from a higher-density inner-disk region and not from the inner edge of the cavity. The absence of further forbidden lines, including no ionized lines, suggests that we are not tracing a photoevaporative wind from the outer cavity wall.

4.2. [O I] Intensity

Figure 4 shows the comparison between the measured accretion luminosity of the sample of Class II stars versus the line luminosity of the [O I] 6300 Å. We include an upper limit to the accretion luminosity measurement of PDS 70, since we use our measurement from the average combined HARPS spectra, but this may be lower during some phases as previously mentioned. PDS 70 appears to be an outlier from both the TD and WTTS samples, with high [O I] line luminosity for the determined accretion luminosity, suggesting the wind is substantial compared to the infall of accreting material. If the same scaling relations were used, the measured [O I] line luminosity of PDS 70 would correspond to an accretion luminosity of $\log(L_{acc}/L_\odot) \approx -1.5$, almost 2 orders of magnitude higher than the accretion luminosity we measure.

Fang et al. (2023) showed that the disks from Upper Sco have, on average, lower accretion and [O I] line luminosities than samples of younger YSOs, but with roughly the same spread in values observed. Hence, PDS 70 is still an outlier in this regard. While the accretion rate of PDS 70 is typical for the sample of other TDs, it is clearly at the high end for what is classed as WTTS (Thanathibodee et al. 2022; Fang et al. 2023). Although, the measured accretion rate when compared to the disk mass of PDS 70 is low in relation to other YSOs (Manara et al. 2019). Comparing the accretion rate we obtain for PDS 70 and the cavity size of ∼60 au, this agrees with the roughly constant relation from other TDs with sizeable cavities, as shown in Manara et al. (2014). It is hence the high [O I] line luminosity that is setting PDS 70 apart from the rest of the sample.

Fang et al. (2023) note only one "bona fide" transition disk in their sample from Upper Sco, which happens to be the other WTTS TD outlier in Figure 4 located above PDS 70. This target is RXJ1604.3-2130A (hereafter, J1604), which is the focus of many previous studies (e.g., Pinilla et al. 2018; Sicilia-Aguilar et al. 2020). J1604 has a misaligned inner disk that casts shadows on the outer disk and is has been a prime candidate for further protoplanet searches, with recent work presenting evidence for a potential companion at the edge of the dust continuum ring (Stadler et al. 2023). We see here that
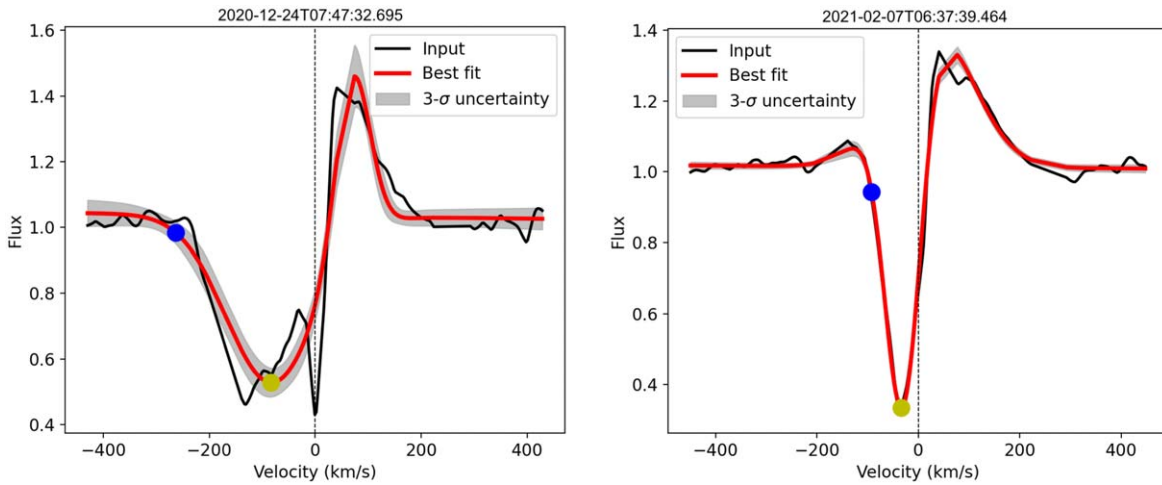
Figure 5. X-Shooter He I 10830 Å line profiles for each epoch of PDS 70 (black). The best composite-model fit is shown in red, with the maximum blueshifted velocity obtained from the 10% depth of the Gaussian absorption fit shown by the blue circles. The maximum depth of the Gaussian component is shown by the yellow circle. Line profiles are photosphere removed and scaled to the local continuum.

it has higher [O I] line luminosity than PDS 70 and a similarly low accretion rate, which has been shown to be highly variable (Sicilia-Aguilar et al. 2020). It does have a much narrower FWHM for the [O I] fit ($\sim$20 km s^{-1}), suggesting a larger Keplerian emitting radius than the inner disk of PDS 70. The other two TDs/WTTSs shown in the lower-left of Figure 4 are 2MASS J16062277-201124 and 2MASS J16151239-2420091. Luhman (2022) classified these as TDs from the WISE SEDs but are non- or faint detections from Atacama Large Millimeter/submillimeter Array surveys (J. Carpenter, private communication). These two targets have some of the lowest measurements for both accretion and [O I] luminosities and may be at the latest stages of disk evolution.

4.3. Variable He I 10830 Å Emission

The other wind-tracing line we detect is He I 10830 Å. Figure 5 shows the photosphere subtracted model fits to this line from each of the X-Shooter epochs. The line has a P-Cygni profile, with the redshifted emission located at approximately the same velocity in each epoch. The blueshifted absorption component, however, displays a significant difference in maximum blueshifted velocity and width. This profile is indicative of tracing stellar/disk winds as He I is self absorbed along our line of sight at the outflow velocity corresponding to the maximum blueshifted values. Taking V_{blue} to be 10% of the maximum depth below the continuum for that Gaussian component (as detailed for inverse P-Cygni profiles and V_{red} in Campbell-White et al. 2021), we obtain values of V_{blue} of -277 and -94 km s^{-1} for epochs 1 and 2, respectively. These are each below the escape velocity of $\sim$480 km s^{-1} for PDS 70.

The profiles of the He I we observe are different from that of the previous detection of this line in Thanathibodee et al. (2020). There, the line has the blueshifted absorption feature, with a measured V_{blue} of $\sim$-85 km s^{-1}, and estimated mass-loss rate of $\sim$1 $\times$ 10^{-11}$M_\odot$ yr^{-1}, consistent with and MHD inner-disk wind. However, in their previous observation, they detect another absorption feature on the red side of the line, contrary to the redshifted emission we see here. The combination of blue and redshifted absorption is more common for highly accreting CTTS, but uncommon for WTTS stars,

with only around 10% of the WTTS targets in Thanathibodee et al. (2023) showing this profile.

We find that the Hα profiles from the X-Shooter observations do not display the inverse P-Cygni profile that Thanathibodee et al. (2020) showed to be variable, in phase with the stellar rotation. Hence, the previous observation of the He I line presented there is likely during a phase where this type of profile would be observed in the Hα, and He is also present in the infalling accretion column. While this kind of double absorption profile may be rare for low to moderate accretors, it is likely due to the nonaxisymmetric accretion columns along our line of sight to the star and, as we see here, a highly variable feature.

4.4. The Peculiarity of PDS 70

Detection of this significant inner-disk wind from PDS 70 would be unusual given its properties even if there were no confirmed protoplanets in the disk. The [O I] is broader and brighter than in other WTTSs and TDs. The [O I] line luminosity is also high for the typical accretion luminosity of WTTSs, which is not far in excess of chromospheric lines luminosity. However, with conclusive accretion measures including the further emission line luminosities that we present, concurrent with the magnetospheric modeling accounting for chromospheric emission (Thanathibodee et al. 2020), the variable He I profile and the presence of H$_2$ in the inner disk (Skinner & Audard 2022), PDS 70 may in fact be at an earlier stage of disk evolution than previously thought.

But is it the presence of the planets, having carved out the substantial cavity in the disk, which allows for a high [O I] luminosity and inner-disk wind, or is it the disk wind that facilitates the direct detection of the planets? Although we cannot answer this, recent theoretical modeling work that incorporates MHD winds in conjunction with planets of differing masses show that different combinations result in substructures with varying parameters (Wafflard-Fernandez & Lesur 2023). Furthermore, the presence of MHD disk winds can influence the formation and migration of planets in the inner disk (Ogihara et al. 2015). Disk winds have also been observed to be modulated by orbital motions of companions (Fang et al. 2014). Since we show that the inner-disk wind of

PDS 70 is likely MHD in origin (Section 4.1), further work on the interplay between protoplanets and such winds will be fundamental in untangling the sources of disk substructures. Forthcoming theoretical predictions and synthetic observations may allow for more robust links between the forbidden emission we detect and the physical conditions producing it. Since the search for protoplanets in this early stage of disk evolution is still ongoing, it would be worth focusing efforts on targets that have similar disk-wind properties to PDS 70.

5. Conclusions

We present here the first detection of forbidden emission from the inner disk of PDS 70. After photospheric removal, we fit the [O I] 6300 Å line using STAR-MELT, and characterize its properties to compare to further Class II stars. Kinematic analysis of the line shows that it originates from a radius of $\sim$0.1–0.2 au, suggesting of a magnetically driven inner-disk wind, which is supported by the blueshifted peak velocity. The luminosity of the [O I] is high for the measured accretion luminosity, and an outlier when compared to other WTTSs and TDs. We also show that the He I 10830 Å line is highly variable, indicative of both winds and rotating nonaxisymmetric accretion flows. We confirm the accretion rate presented in the literature using a different method, and determine log $(\dot{M}_{acc} \ yr^{-1}) = -10.06 \pm 0.11$ from a selection of accretion tracing emission line luminosities.

We find that PDS 70 still has ongoing accretion from the inner disk, even with no continuum excess observed at UV wavelengths in the X-Shooter observations. The results we find for the substantial inner-disk wind from PDS 70 suggest that it is MHD in origin, and in combination with the dense inner disk is shielding the planets and the outer disk from the photoionization of the central star that was previously inferred from XUV observations. We do not find direct evidence of a photoevaporative wind from either the inner or outer disk. It may be that the significant MHD wind helped to clear out the cavity that was carved by the giant protoplanets, and may have facilitated their direct detections. A similar mechanism could be in play in J1604, allowing the shadows from the inner disk to be cast on the outer disk. It may also be that the enhanced [O I] luminosity and broad profile is the result of the protoplanets significant influence in the disk. Future modeling work on disentangling the effects of planets and winds may help to reconcile these and future observations as we search for further protoplanets around young stars.

Appendix A
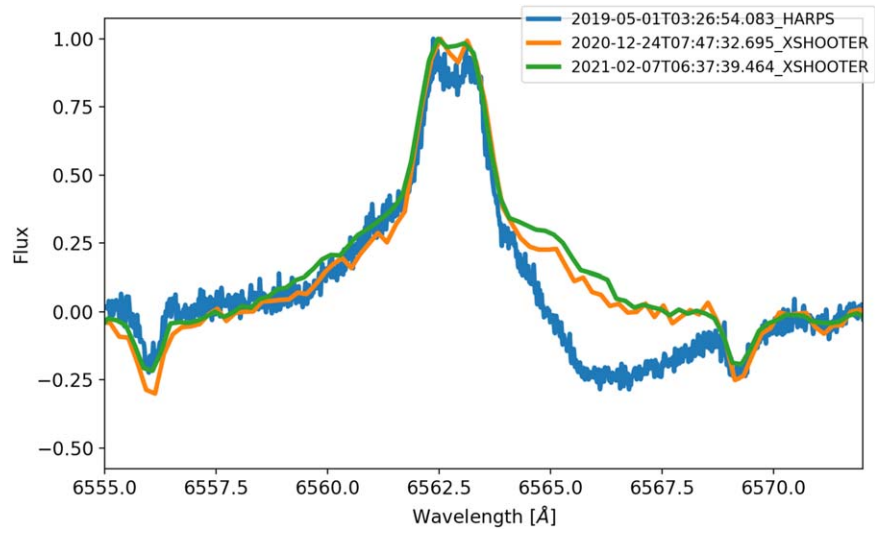## X-Shooter Observations

Figure 6 shows the two X-Shooter observations of PDS 70, combining each wavelength range, UV-blue ($\sim$300–560 nm), visible ($\sim$560–1024 nm), and NIR ($\sim$1020–2480 nm). Observations were taken in service mode on 2020 December 24 and 2021 February 7, each with clear conditions and seeing $<2''$. These used a combination of short exposures (45–108 s) with the wide-slit setups ($5{.}''0$) to measure absolute fluxes, and longer exposures (320–600 s) with nod-on-slit integration, with slit widths of $1{.}''0/0{.}''4/0{.}''4$, achieving spectral resolutions of R $\sim$ 5400, 18,400, and 11,600 in the three respective wavelength ranges. The spectra were reduced using the ESO-Reflex (Freudling et al. 2013) X-Shooter pipeline v3.5.0 (Modigliani et al. 2010) and telluric lines were removed using molecfit (Smette et al. 2015; Kausch et al. 2015). The final flux calibration was performed by rescaling the flux of the narrow slit to that of the wide slit, as described by Manara et al. (2021).

Figure 7 shows the Hα profiles of each X-Shooter observation, as well as a comparison HARPS spectra featuring the inverse P-Cygni type profile not observed in the X-Shooter epochs. Here the flux has been normalized and continuum subtracted for comparison between instruments.
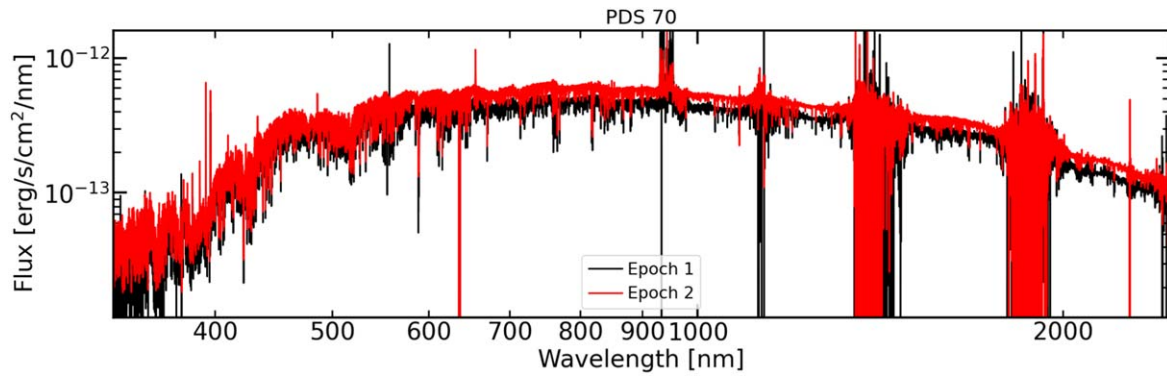
Figure 6. X-Shooter spectra of PDS70. Epoch 1: 2020-12-24T07:47:32.695. Epoch 2: 2021-02-07T06:37:39.464.

Figure 7. X-Shooter and an example HARPS spectra of PDS70 Hα profile. Flux is normalized and continuum subtracted.

8

Appendix B
HARPS Observing Log

Table 1 outlines the HARPS observations used in this work.

Table 1
Observation Log of HARPS Exposures of PDS 70

UTC	MJD	Exp. Time (s)	UTC	MJD	Exp. Time (s)
2018-03-29T06:33:21.929	58,206.273170	899	2018-04-22T05:25:12.656	58,230.225841	1799
2018-03-29T06:48:53.411	58,206.283952	899	2018-04-23T04:50:54.677	58,231.202022	1799
2018-03-29T07:04:24.412	58,206.294727	899	2018-05-01T04:29:40.280	58,239.187272	1799
2018-03-29T07:19:55.403	58,206.305502	899	2018-05-01T05:00:11.202	58,239.208463	1799
2018-03-29T07:36:39.719	58,206.317126	899	2018-05-06T03:28:07.285	58,244.144529	1799
2018-03-29T07:52:10.410	58,206.327898	899	2018-05-06T03:58:38.487	58,244.165723	1799
2018-03-30T05:41:37.995	58,207.237245	899	2018-05-13T05:09:56.831	58,251.215241	1799
2018-03-30T05:57:09.426	58,207.248026	899	2018-05-13T05:40:27.781	58,251.236433	1799
2018-03-30T06:12:40.418	58,207.258801	899	2019-02-13T08:32:20.542	58,527.355793	1799
2018-03-30T08:22:46.841	58,207.349153	899	2019-02-13T09:02:50.943	58,527.376979	1799
2018-03-30T08:38:17.403	58,207.359924	899	2019-05-01T03:26:54.083	58,604.143682	2398
2018-03-30T08:53:48.465	58,207.370700	899	2019-05-01T04:07:23.607	58,604.171801	2398
2018-03-31T03:39:16.712	58,208.152277	899	2020-02-27T05:23:41.660	58,906.224788	1799
2018-03-31T03:54:47.424	58,208.163049	899	2020-02-29T05:14:52.221	58,908.218660	1799
2018-03-31T06:35:19.070	58,208.274526	899	2020-02-29T05:45:23.028	58,908.239850	1799
2018-03-31T06:50:49.412	58,208.285294	899	2020-03-12T05:12:57.551	58,920.217333	1799
2018-03-31T08:28:24.178	58,208.353058	899	2020-03-12T06:02:39.146	58,920.251842	1799
2018-03-31T08:43:55.479	58,208.363837	899	2020-03-13T04:36:00.448	58,921.191672	1799
2018-04-18T05:12:34.801	58,226.217069	1799	2020-03-13T05:06:32.210	58,921.212873	1799
2018-04-19T05:04:01.821	58,227.211132	899	2020-03-14T06:32:01.043	58,922.272234	1799
2018-04-19T05:19:33.003	58,227.221910	899	2020-03-14T07:02:32.253	58,922.293429	1799
2018-04-20T05:19:03.239	58,228.221565	1799	2020-03-15T04:16:16.025	58,923.177963	1799
2018-04-20T05:49:35.891	58,228.242777	1799	2020-03-15T04:46:47.164	58,923.199157	1799
2018-04-21T05:51:29.173	58,229.244088	1799	…	…	…

Appendix C
Accretion Luminosity

Accurate measurement of the line fluxes required subtracting the photospheric absorption features from the PDS 70 spectra. We used a HARPS main-sequence K7 star template, HD35650, since Class III templates can still have significant chromospheric emission from these accretion tracing lines. The Hδ line had the most significant photospheric contamination around the emission line, but we were able to adequately remove this to estimate the line flux, albeit with higher uncertainties than the other emission lines.

We measured the EWs of the continuum normalized, higher-resolution HARPS spectra. We took the mean continuum absolute flux values from the two calibrated X-Shooter observations around each line. Multiplying these quantities hence provided absolute integrated flux for each emission line. This allowed for the luminosities of each emission line to be determined, using the distance of 112.4 pc (Gaia Collaboration et al. 2021). Line luminosities were then converted to accretion luminosities following the Alcalá et al. (2017) relations. These results are summarized in Table 2.

Table 2
Flux Calculated from Median Combined Photosphere Removed HARPS Spectra, Using the Average X-Shooter Continuum Flux

	Hα	Hβ	Hγ	Hδ	Ca II (H)	Ca II (K)
Continuum Flux (10^{-13} erg s^{-1} cm^{-2} nm^{-1})	5.25 ± 0.07	3.13 ± 0.11	2.25 ± 0.12	1.21 ± 0.35	0.65 ± 0.18	0.55 ± 0.11
Integrated Flux (10^{-14} erg s^{-1} cm^{-2})	19.9 ± 0.01	3.91 ± 0.03	1.47 ± 0.12	1.82 ± 0.55	2.07 ± 0.27	3.55 ± 0.13
Line Luminosity log ($L_{line}/L_\odot$)	-4.10 ± 0.03	-4.81 ± 0.04	-5.24 ± 0.08	-5.14 ± 0.18	-5.09 ± 0.09	-4.85 ± 0.06
Accretion Luminosity log ($L_{acc}/L_\odot$)	-2.90 ± 0.06	-2.90 ± 0.08	-3.09 ± 0.17	-2.86 ± 0.28	-2.74 ± 0.18	-2.79 ± 0.17
Accretion Rate log ($M_\odot$ yr^{-1})	-10.08 ± 0.11	-10.08 ± 0.11	-10.27 ± 0.11	-10.04 ± 0.11	-9.92 ± 0.11	-9.97 ± 0.11

Note. Corresponding line luminosities are shown with accretion luminosities from Alcalá et al. (2017) correlations.

ORCID iDs

Justyn Campbell-White ⓘ https://orcid.org/0000-0002-3913-3746
Carlo F. Manara ⓘ https://orcid.org/0000-0003-3562-262X
Myriam Benisty ⓘ https://orcid.org/0000-0002-7695-7605
Rik A. B. Claes ⓘ https://orcid.org/0000-0001-8194-4238
Antonio Frasca ⓘ https://orcid.org/0000-0002-0474-0896
Jaehan Bae ⓘ https://orcid.org/0000-0001-7258-770X
Stefano Facchini ⓘ https://orcid.org/0000-0003-4689-2684
Andrea Isella ⓘ https://orcid.org/0000-0001-8061-2207
Laura Pérez ⓘ https://orcid.org/0000-0002-1199-9564
Paola Pinilla ⓘ https://orcid.org/0000-0001-8764-1780
Aurora Sicilia-Aguilar ⓘ https://orcid.org/0000-0002-8421-0851
Richard Teague ⓘ https://orcid.org/0000-0003-1534-5186

References

Alcalá, J. M., Manara, C. F., Natta, A., et al. 2017, A&A, 600, A20
Alexander, R., Pascucci, I., Andrews, S., Armitage, P., & Cieza, L. 2014, in Protostars and Planets VI, ed. H. Beuther et al. (Tucson, AZ: Univ. Arizona Press), 475
Andrews, S. M. 2020, ARA&A, 58, 483
Aoyama, Y., & Bai, X.-N. 2023, ApJ, 946, 5
Bae, J., Isella, A., Zhu, Z., et al. 2022, arXiv:2210.13314
Banzatti, A., Pascucci, I., Edwards, S., et al. 2019, ApJ, 870, 76
Banzatti, A., & Pontoppidan, K. M. 2015, ApJ, 809, 167
Benisty, M., Bae, J., Facchini, S., et al. 2021, ApJL, 916, L2
Benisty, M., Dominik, C., Follette, K., et al. 2022, arXiv:2203.09991
Campbell-White, J., Sicilia-Aguilar, A., Manara, C. F., et al. 2021, MNRAS, 507, 3331
Ercolano, B., & Owen, J. E. 2010, MNRAS, 406, 1553
Ercolano, B., & Picogna, G. 2022, EPJP, 137, 1357
Erkal, J., Manara, C. F., Schneider, P. C., et al. 2022, A&A, 666, A188
Fang, M., Pascucci, I., Edwards, S., et al. 2018, ApJ, 868, 28
Fang, M., Pascucci, I., Edwards, S., et al. 2023, ApJ, 945, 112
Fang, M., Sicilia-Aguilar, A., Roccatagliata, V., et al. 2014, A&A, 570, A118
Flock, M., Fromang, S., Turner, N. J., & Benisty, M. 2017, ApJ, 835, 230
Freudling, W., Romaniello, M., Bramich, D. M., et al. 2013, A&A, 559, A96
Gaia Collaboration, Brown, A. G. A., Vallenari, A., et al. 2021, A&A, 649, A1
Gárate, M., Delage, T. N., Stadler, J., et al. 2021, A&A, 655, A18
Gregorio-Hetem, J., & Hetem, A. 2002, MNRAS, 336, 197
Haffert, S. Y., Bohn, A. J., de Boer, J., et al. 2019, NatAs, 3, 749
Hartigan, P., Edwards, S., & Ghandour, L. 1995, ApJ, 452, 736

Joyce, S. R. G., Pye, J. P., Nichols, J. D., et al. 2020, MNRAS, 491, L56
Joyce, S. R. G., Pye, J. P., Nichols, J. D., et al. 2023, MNRAS, 519, 4514
Kausch, W., Noll, S., Smette, A., et al. 2015, A&A, 576, A78
Keppler, M., Benisty, M., Müller, A., et al. 2018, A&A, 617, A44
Lodato, G., Dipierro, G., Ragusa, E., et al. 2019, MNRAS, 486, 453
Luhman, K. L. 2022, AJ, 163, 25
Manara, C. F., Beccari, G., Da Rio, N., et al. 2013a, A&A, 558, A114
Manara, C. F., Testi, L., Rigliaco, E., et al. 2013b, A&A, 551, A107
Manara, C. F., Frasca, A., Venuti, L., et al. 2021, A&A, 650, A196
Manara, C. F., Mordasini, C., Testi, L., et al. 2019, A&A, 631, L2
Manara, C. F., Testi, L., Natta, A., et al. 2014, A&A, 568, A18
Mayor, M., Pepe, F., Queloz, D., et al. 2003, Msngr, 114, 20
McGinnis, P., Dougados, C., Alencar, S. H. P., Bouvier, J., & Cabrit, S. 2018, A&A, 620, A87
Modigliani, A., Goldoni, P., Royer, F., et al. 2010, Proc. SPIE, 7737, 773728
Müller, A., Keppler, M., Henning, T., et al. 2018, A&A, 617, L2
Natta, A., Testi, L., Alcalá, J. M., et al. 2014, A&A, 569, A5
Nemer, A., Goodman, J., & Wang, L. 2020, ApJL, 904, L27
Nisini, B., Antoniucci, S., Alcalá, J. M., et al. 2018, A&A, 609, A87
Ogihara, M., Kobayashi, H., Inutsuka, S.-i., & Suzuki, T. K. 2015, A&A, 579, A65
Owen, J. E. 2016, PASA, 33, e005
Pascucci, I., Cabrit, S., Edwards, S., et al. 2023, in ASP Conf. Ser. 534, Protostars and Planets VII, ed. S. Inutsuka et al. (San Francisco, CA: ASP), 567
Pecaut, M. J., & Mamajek, E. E. 2016, MNRAS, 461, 794
Perotti, G., Christiaens, V., Henning, T., et al. 2023, Natur, 620, 516
Picogna, G., Ercolano, B., Owen, J. E., & Weber, M. L. 2019, MNRAS, 487, 691
Pinilla, P., Benisty, M., de Boer, J., et al. 2018, ApJ, 868, 85
Rigliaco, E., Pascucci, I., Gorti, U., Edwards, S., & Hollenbach, D. 2013, ApJ, 772, 60
Riols, A., & Lesur, G. 2019, A&A, 625, A108
Riols, A., Lesur, G., & Menard, F. 2020, A&A, 639, A95
Sicilia-Aguilar, A., Manara, C. F., de Boer, J., et al. 2020, A&A, 633, A37
Simon, M. N., Pascucci, I., Edwards, S., et al. 2016, ApJ, 831, 169
Skinner, S. L., & Audard, M. 2022, ApJ, 938, 134
Smette, A., Sana, H., Noll, S., et al. 2015, A&A, 576, A77
Stadler, J., Benisty, M., Izquierdo, A., et al. 2023, A&A, 670, L1
Takahashi, S. Z., & Muto, T. 2018, ApJ, 865, 102
Thanathibodee, T., Calvet, N., Hernández, J., Maucó, K., & Briceño, C. 2022, AJ, 163, 74
Thanathibodee, T., Molina, B., Calvet, N., et al. 2020, ApJ, 892, 81
Thanathibodee, T., Molina, B., Serna, J., et al. 2023, ApJ, 944, 90
Vernet, J., Dekker, H., D'Odorico, S., et al. 2011, A&A, 536, A105
Wafflard-Fernandez, G., & Lesur, G. 2023, A&A, 677, A70
Weber, M. L., Ercolano, B., Picogna, G., Hartmann, L., & Rodenkirch, P. J. 2020, MNRAS, 496, 223